

1**Evaluation of autoconversion and accretion enhancement factors in GCM warm-rain**  
2**parameterizations using ground-based measurements at the Azores**

3Peng Wu<sup>1</sup>, \*Baiké Xi<sup>1</sup>, Xiquan Dong<sup>1</sup>, and Zhibo Zhang<sup>2</sup>

4<sup>1</sup> Department of Hydrology and Atmospheric Sciences, The University of Arizona, Tucson,  
5Arizona, USA

6<sup>2</sup> Physics Department, The University of Maryland, Baltimore County, Maryland, USA

7

8

9 Submitted to Atmospheric Chemistry and Physics (September 17, 2018)

10

11

12**Keywords:** MBL clouds, enhancement factors, autoconversion and accretion parameterizations

13

14

15

16

17

18\* Corresponding author address: Dr. Baiké Xi, Department of Hydrology and Atmospheric  
19Sciences, University of Arizona, 1133 E. James E. Rogers Way, Tucson, AZ 85721-0011.  
20baikexi@email.arizona.edu; Phone: 520-626-8945

## Abstract

A great challenge in climate modelling is how to parametrize sub-grid cloud processes, such as autoconversion and accretion in warm rain formation. In this study, we use ground-based observations and retrievals over the Azores to investigate the so-called enhancement factors,  $E_{auto}$  and  $E_{accr}$ , which are often used in climate models to account for the influences of sub-grid variances of cloud and precipitation water on the autoconversion and accretion processes.  $E_{auto}$  and  $E_{accr}$  are computed for different model resolutions. The calculated  $E_{auto}$  values increase from 1.96 (30 km) to 3.15 (120 km), and the calculated  $E_{accr}$  values increase from 1.53 (30 km) to 1.76 (180 km). Comparing the prescribed enhancement factors in Morrison and Gettleman (2008, MG08) to the observed ones, we found that a higher  $E_{auto}$  (3.2) at small grids and lower  $E_{accr}$  (1.07) are used in MG08, which helps to explain why most of the GCMs produce too frequent precipitation events but with too light precipitation intensity. The ratios of rain to cloud water mixing ratio at  $E_{accr}=1.07$  and  $E_{accr}=2.0$  are 0.063 and 0.142, respectively, further proving that the prescribed value of  $E_{accr}=1.07$  used in MG08 is too small to simulate correct precipitation intensity. Both  $E_{auto}$  and  $E_{accr}$  increase when the boundary layer becomes less stable, and the values are larger in precipitating clouds ( $CLWP > 75 \text{ gm}^{-2}$ ) than those in nonprecipitating clouds ( $CLWP < 75 \text{ gm}^{-2}$ ). Therefore, the selection of  $E_{auto}$  and  $E_{accr}$  values in GCMs should be regime-dependent.

## 1. Introduction

Due to their vast areal coverage (Warren et al., 1986, 1988; Hahn and Warren, 2007) and strong radiative cooling effect (Hartmann et al., 1992; Chen et al., 2000), small changes in the coverage or thickness of marine boundary layer (MBL) clouds could change the radiative energy budget significantly (Hartmann and Short, 1980; Randall et al., 1984) or even offset the radiative effects produced by increasing greenhouse gases (Slingo, 1990). The lifetime of MBL clouds remains an issue in climate models (Yoo and Li, 2012; Jiang et al., 2012; Yoo et al., 2013; Stanfield et al., 2014) and represents one of the largest uncertainties in predicting future climate (Wielicki et al., 1995; Houghton et al., 2001; Bony and Dufresne, 2005).

MBL clouds frequently produce precipitation, mostly in the form of drizzle (Austin et al., 1995; Wood, 2005a; Leon et al., 2008; Wood, 2012). A significant amount of drizzle is evaporated before reaching the surface, for example, about ~76% over the Azores region in Northeast Atlantic (Wu et al., 2015), which provides another water vapour source for MBL clouds. Due to their pristine environment and their close vicinity to the surface, MBL clouds are especially sensitive to aerosol perturbations (Quaas et al., 2009; Kooperman et al., 2012). Most aerosol indirect effects are associated with precipitation suppression (Albrecht, 1989; Ackerman et al., 2004; Lohmann and Feichter, 2005; Wood, 2007). Thus, accurate prediction of precipitation is essential in simulating the global energy budget and in constraining aerosol indirect effects in climate projections.

Due to the coarse spatial resolutions of the general circulation model (GCM) grid, many cloud processes cannot be adequately resolved and must be parameterized. For example, warm rain parameterizations in most GCMs treat the condensed water as either cloud or rain from the collision-coalescence process, which is partitioned into autoconversion and accretion sub-processes in model parameterizations (Kessler, 1969; Tripoli and Cotton, 1980; Beheng, 1994; Khairoutdinov and Kogan, 2000; Liu and Daum, 2004). Autoconversion represents the process that drizzle drops being formed through the condensation of cloud droplets and accretion represents the process where rain drops grow by the coalescence of drizzle-sized drops with cloud droplets. Autoconversion mainly accounts for precipitation initiation while accretion primarily contributes to precipitation intensity. Autoconversion is often parameterized as functions of cloud droplet number concentration ( $N_c$ ) and cloud water mixing ratio ( $q_c$ ), while accretion depends on both cloud and rain water mixing ratios ( $q_c$  and  $q_r$ ) (Kessler, 1969; Tripoli and Cotton, 1980; Beheng, 1994; Khairoutdinov and Kogan, 2000; Liu and Daum, 2004; Wood, 2005b). All previous studies suggested that these two processes as power law functions of cloud and precipitation properties (See section 2 for details).

In conventional GCMs, the lack of information on the sub-grid variances of cloud and precipitation leads to the unavoidable use of the grid-mean quantities ( $\overline{N_c}$ ,  $\overline{q_c}$ , and  $\overline{q_r}$ , where overbar denotes grid mean, same below) in calculating autoconversion and accretion rates. MBL cloud liquid water path (CLWP) distributions are often positive skewed (Wood and

Hartmann, 2006; Dong et al., 2014a and 2014b), that is, the mean value is greater than mode value. Thus, the mean value only represents a relatively small portion of samples. Also, due to the nonlinear nature of the relationships, the two processes depend significantly on the sub-grid variability and co-variability of cloud and precipitation microphysical properties (Weber and Quass, 2012; Boutle et al., 2014). In some GCMs, sub-grid scale variability is often ignored or hard coded using constants to represent the variabilities under all meteorological conditions and across the entire globe (Pincus and Klein, 2000; Morrison and Gettleman, 2008; Lebsock et al., 2013). This could lead to systematic errors in precipitation rate simulations (Wood et al., 2002; Larson et al., 2011; Lebsock et al., 2013; Boutle et al., 2014; Song et al., 2018), where GCMs are found to produce too frequent but too light precipitation compared to observations (Zhang et al., 2002; Jess, 2010; Stephens et al., 2010; Nam and Quaas, 2012; Song et al., 2018). The bias is found to be smaller by using a probability density function (PDF) of cloud water to represent the sub-grid scale variability in autoconversion parameterization (Beheng, 1994; Zhang et al., 2002; Jess, 2010), or more complexly, by integrating the autoconversion rate over a joint PDF of liquid water potential temperature, vertical velocity, total water mixing ratio and rain water mixing ratio (Cheng and Xu, 2009).

Process rate enhancement factors ( $E$ ) are introduced when considering sub-grid scale variability in parameterizing grid-mean processes and they should be parameterized as functions of the PDFs of cloud and precipitation properties within a grid box (Morrison and

97 Gettleman, 2008; Lebsock et al., 2013; Boutle et al., 2014). However, these values in some  
98 GCM parameterization schemes are prescribed as constants regardless of underlying surface  
99 or meteorological conditions (Xie and Zhang, 2015). Boutle et al. (2014) used aircraft in situ  
100 measurements and remote sensing techniques to develop a parameterization for cloud and rain,  
101 in which not only consider the sub-grid variabilities under different grid scales, but also  
102 consider the variation of cloud and rain fractions. The parameterization was found to reduce  
103 precipitation estimation bias significantly. Hill et al. (2015) modified this parameterization and  
104 developed a regime and cloud type dependent sub-grid parameterization, which was  
105 implemented to the Met Office Unified Model by Walters et al. (2017) and found that the  
106 radiation bias is reduced using the modified parameterization. Using ground-based  
107 observations and retrievals, Xie and Zhang (2015) proposed a scale-aware cloud  
108 inhomogeneity parameterization that they applied to the Community Earth System Model  
109 (CESM) and found that it can recognize spatial scales without manual tuning. The  
110 inhomogeneity parameter is essential in calculating enhancement factors and affect the  
111 conversion rate from cloud to rain liquid. Xie and Zhang (2015), however, did not evaluate the  
112 validity of CESM simulations from their parameterization; the effect of  $N_c$  variability or the  
113 effect of covariance of cloud and rain on accretion process was not assessed. Most recently,  
114 Zhang et al. (2018) derived the sub-grid CLWP and  $N_c$  from the MODIS cloud product. They  
115 also studied the implication of the sub-grid cloud property variations for the autoconversion

116 rate simulation, in particular the enhancement factor, in GCMs. For the first time, the  
117 enhancement factor due to the sub-grid variation of  $N_c$  is derived from satellite observation,  
118 and results reveal several regions downwind of biomass burning aerosols (e.g., Gulf of Guinea,  
119 East Coast of South Africa), air pollution (i.e., Eastern China Sea), and active volcanos (e.g.,  
120 Kilauea Hawaii and Ambae Vanuatu), where the enhancement factor due to  $N_c$  is comparable,  
121 or even larger than that due to CLWP. However, one limitation of Zhang et al. (2018) is the  
122 use of passive remote sensing data only, which cannot distinguish cloud and rain water.

123 Dong et al. (2014a and 2014b) and Wu et al. (2015) reported MBL cloud and rain properties  
124 over the Azores and provided the possibility of calculating the enhancement factors using  
125 ground-based observations and retrievals. A joint retrieval method to estimate  $q_c$  and  $q_r$  profiles  
126 is proposed based on existing studies and is presented in Appendix A. Most of the calculations  
127 and analyses in this study is based on Morrison and Gettleman (2008, MG08 hereafter) scheme.  
128 The enhancement factors in several other schemes are also discussed and compared with the  
129 observational results and the approach in this study can be repeated for other microphysics  
130 schemes in GCMs. This manuscript is organized as follows: section 2 includes a summary of  
131 the mathematical formulas from previous studies that can be used to calculate grid-mean  
132 process enhancement factors. Ground-based observations and retrievals are introduced in  
133 Section 3. Section 4 presents results and discussions, followed by summary and conclusions in  
134 Section 5. The retrieval method used in this study is in Appendix A.

## 135 2. Mathematical Background

136 Autoconversion and accretion rates in GCMs are usually parameterized as power law  
 137 equations (Tripoli and Cotton, 1980; Beheng, 1994; Khairoutdinov and Kogan, 2000; Liu and  
 138 Daum, 2004):

$$139 \left( \frac{\partial q_r}{\partial t} \right)_{auto} = A \bar{q}_c^{a1} \bar{N}_c^{a2}, \quad (1)$$

$$140 \left( \frac{\partial q_r}{\partial t} \right)_{accr} = B (\bar{q}_c \bar{q}_r)^b, \quad (2)$$

141 where  $A$ ,  $a1$ ,  $a2$ ,  $B$ , and  $b$  are coefficients in different schemes listed in Table 1. The  $\bar{q}_c$ ,  $\bar{q}_r$ ,  
 142 and  $\bar{N}_c$  are grid-mean cloud water mixing ratio, rain water mixing ratio, and droplet number  
 143 concentration, respectively. Because it is widely used in model parameterizations, the detailed  
 144 results from Khairoutdinov and Kogan (2000) parameterization that been used in MG08  
 145 scheme will be shown in Section 4 while a summary will be given for other schemes.

146 Ideally, the covariance between physical quantities should be considered in the calculation  
 147 of both processes. However,  $\bar{q}_c$  and  $\bar{N}_c$  in Eq. (1) are arguably not independently retrieved in  
 148 our retrieval method which will be introduced in this section and Appendix A. Thus we only  
 149 assess the individual roles of  $q_c$  and  $N_c$  sub-grid variations in determining autoconversion rate.  
 150  $q_c$  and  $q_r$ , on the other hand, are retrieved from two independent algorithms as shown in Dong  
 151 et al. (2014a and 2014b), Wu et al. (2015) and Appendix A, we will assess the effect of cloud  
 152 and rain property covariance on accretion rate calculations.



153 In the sub-grid scale, the PDFs of  $q_c$  and  $N_c$  are assumed to follow a gamma distribution  
 154 based on observational studies of optical depth in MBL clouds (Barker et al., 1996; Pincus et  
 155 al., 1999; Wood and Hartmann, 2006):

$$156 \quad P(x) = \frac{\alpha^\nu}{\Gamma(\nu)} x^{\nu-1} e^{-\alpha x}, \quad (3)$$

157 where  $x$  represents  $q_c$  or  $N_c$  with grid-mean quantity  $\bar{q}_c$  or  $\bar{N}_c$ , represented by  $\mu$ ,  $\alpha = \nu/\mu$  is the  
 158 scale parameter,  $\sigma^2$  is the relative variance of  $x$  (= variance divided by  $\mu^2$ ),  $\nu = 1/\sigma^2$  is the  
 159 shape parameter.  $\nu$  is an indicator of cloud field homogeneity, with large values representing  
 160 homogeneous and small values indicating inhomogeneous cloud field.

161 By integrating autoconversion rate, Eq. (1), over the grid-mean rate, Eq. (3), with respect  
 162 to sub-grid scale variation of  $q_c$  and  $N_c$ , the autoconversion rate can be expressed as:

$$163 \quad \left( \frac{\partial q_r}{\partial t} \right)_{auto} = A \mu_{q_c}^{a1} \mu_{N_c}^{a2} \frac{\Gamma(\nu+a)}{\Gamma(\nu) \nu^a}, \quad (4)$$

164 where  $a = a1$  or  $a2$ . Comparing Eq. (4) to Eq. (1), the autoconversion enhancement factor  
 165 ( $E_{auto}$ ) can be given with respect to  $q_c$  and  $N_c$ :

$$166 \quad E_{auto} = \frac{\Gamma(\nu+a)}{\Gamma(\nu) \nu^a}. \quad (5)$$

167 In addition to fitting the distributions of  $q_c$  and  $N_c$ , we also tried two other methods to  
 168 calculate  $E_{auto}$ . The first is to integrate Eq. (1) over the actual PDFs from observed or retrieved  
 169 parameters and the second is to fit a lognormal distribution for sub-grid variability like what  
 170 has been done in other studies (e.g., Lebsock et al., 2013; Larson and Griffin, 2013). It is found

171 that all three methods get similar results. In this study, we use a gamma distribution that is  
 172 consistent with MG08. Also note that, in the calculation of  $E_{auto}$  from  $\overline{N_c}$ , the negative exponent  
 173 (-1.79) may cause singularity problems in Eq. (5). When this situation occurs, we do direct  
 174 calculations by integrating the PDF of  $\overline{N_c}$  rather than using Eq. (5).

175 To account for the covariance of microphysical quantities in a model grid, it is difficult to  
 176 apply bivariate gamma distribution due to its complex nature. In this study, the bivariate  
 177 lognormal distribution of  $q_c$  and  $q_r$  is used (Lebsock et al., 2013; Boutle et al., 2014) and can  
 178 be written as:

$$\begin{aligned}
 179 \quad P(\overline{q_c}, \overline{q_r}) &= \frac{1}{2\pi\overline{q_c}\overline{q_r}\sigma_{q_c}\sigma_{q_r}\sqrt{1-\rho^2}} \exp \left\{ -\frac{1}{2} \frac{1}{1-\rho^2} \left[ \left( \frac{\ln\overline{q_c} - \mu_{q_c}}{\sigma_{q_c}} \right)^2 - 2\rho \left( \frac{\ln\overline{q_c} - \mu_{q_c}}{\sigma_{q_c}} \right) \left( \frac{\ln\overline{q_r} - \mu_{q_r}}{\sigma_{q_r}} \right) + \right. \right. \\
 180 \quad &\left. \left. \left( \frac{\ln\overline{q_r} - \mu_{q_r}}{\sigma_{q_r}} \right)^2 \right] \right\}, \tag{6}
 \end{aligned}$$

181 where  $\sigma$  is standard deviation and  $\rho$  is the correlation coefficient of  $q_c$  and  $q_r$ .

182 Similarly, by integrating the accretion rate in Eq. (2) from Eq. (6), we get the accretion  
 183 enhancement factor ( $E_{accr}$ ) of:

$$184 \quad E_{accr} = \left(1 + \frac{1}{v_{q_c}}\right)^{\frac{1.15^2 - 1.15}{2}} \left(1 + \frac{1}{v_{q_r}}\right)^{\frac{1.15^2 - 1.15}{2}} \exp(\rho 1.15^2 \sqrt{\ln\left(1 + \frac{1}{v_{q_c}}\right) \ln\left(1 + \frac{1}{v_{q_r}}\right)}). \tag{7}$$

### 3. Ground-based observations and retrievals

The datasets used in this study were collected at the Department of Energy (DOE) Atmospheric Radiation Measurement (ARM) Mobile Facility (AMF), which was deployed on the northern coast of Graciosa Island (39.09°N, 28.03°W) from June 2009 to December 2010 (for more details, please refer to Rémillard et al., 2012; Dong et al., 2014a and Wood et al., 2015). The detailed operational status of the remote sensing instruments on AMF was summarized in Figure 1 of Rémillard et al. (2012) and discussed in Wood et al. (2015). The ARM Eastern North Atlantic (ENA) site was established on the same island in 2013 and provides long-term continuous observations.

The cloud-top heights ( $Z_{\text{top}}$ ) were determined from W-band ARM cloud radar (WACR) reflectivity and only single-layered low-level clouds with  $Z_{\text{top}} \leq 3$  km are selected. Cloud-base heights ( $Z_{\text{base}}$ ) were detected by a laser ceilometer (CEIL) and the cloud thickness was simply the difference between cloud top and base heights. The cloud liquid water path (CLWP) was retrieved from microwave radiometer (MWR) brightness temperatures measured at 23.8 and 31.4 GHz using a statistical retrieval method with an uncertainty of  $20 \text{ g m}^{-2}$  for  $\text{CLWP} < 200 \text{ g m}^{-2}$ , and 10% for  $\text{CLWP} > 200 \text{ g m}^{-2}$  (Liljegren et al., 2001; Dong et al., 2000). Precipitating status is identified through a combination of WACR reflectivity and  $Z_{\text{base}}$ . As in Wu et al. (2015), we labelled the status of a specific time as “precipitating” if the WACR reflectivity below the cloud base exceeds -37 dBZ.

204 The ARM merged sounding data have a 1-min temporal and 20-m vertical resolution below  
 205 3 km (Troyan, 2012). In this study, the merged sounding profiles are averaged to 5-min  
 206 resolution. Pressure and temperature profiles are used to calculate air density ( $\rho_{air}$ ) profiles  
 207 and to infer adiabatic cloud water content.

208 Cloud droplet number concentration ( $N_c$ ) is retrieved using the methods presented in Dong  
 209 et al. (1998, 2014a and 2014b) and are assumed to be constant in a cloud layer. Vertical profiles  
 210 of cloud and rain water content (CLWC and RLWC) are retrieved by combining WACR  
 211 reflectivity, CEIL attenuated backscatter and by assuming adiabatic growth of cloud parcels.  
 212 The detailed description is presented in Appendix A with the results from a selected case. The  
 213 CLWC and RLWC values are transformed to  $q_c$  and  $q_r$  by dividing by air density (e.g.,  $q_c(z) =$   
 214  $CLWC(z)/\rho_{air}(z)$ ).

215 The estimated uncertainties for the retrieved  $q_c$  and  $q_r$  are 30% and 18%, respectively (see  
 216 Appendix A). We used the estimated uncertainties of  $q_r$  and  $q_c$  as inputs of Eqs. (4) and (7) to  
 217 assess the uncertainties of  $E_{auto}$  and  $E_{accr}$ . For instance,  $(1 \pm 0.3)q_c$  are used in Eq. (4) and the  
 218 mean differences are then used as the uncertainty of  $E_{auto}$ . Same method is used to estimate the  
 219 uncertainty for  $E_{accr}$ .

220 The autoconversion and accretion parameterizations partitioned from the collision-  
 221 coalescence process dominate at different levels in a cloud layer. Autoconversion dominates  
 222 around cloud top where cloud droplets reach maximum by condensation and accretion is

223 dominant at middle and lower parts of the cloud where rain drops sediment and continue to  
224 grow by collecting cloud droplets. Complying with the physical processes, we estimate  
225 autoconversion and accretion rates at different levels of a cloud layer in this study. The  
226 averaged  $q_c$  within the top five range gates (~215 m thick) are used to calculate  $E_{auto}$ . To  
227 calculate  $E_{accr}$ , we use the averaged  $q_c$  and  $q_r$  within five range gates around the maximum  
228 radar reflectivity. If the maximum radar reflectivity appears at the cloud base, then five range  
229 gates above the cloud base are used.

230 The ARM merged sounding data are also used to calculate lower tropospheric stability  
231 ( $LTS = \theta_{700 \text{ hPa}} - \theta_{1000 \text{ hPa}}$ ), which is used to infer the boundary layer stability. In this study,  
232 unstable and stable boundary layers are defined as LTS less than 13.5 K and greater than 18 K,  
233 respectively, and environment with an LTS between 13.5 K and 18 K is defined as mid-stable  
234 (Wang et al. 2012; Bai et al. 2018). Enhancement factors in different boundary layers are  
235 summarized in Section 4.2 and may be used as references for model simulations. Further, two  
236 regimes are classified: CLWP greater than  $75 \text{ g m}^{-2}$  as precipitating and CLWP less than  $75 \text{ g}$   
237  $\text{m}^{-2}$  as nonprecipitating (Rémillard et al., 2012).

238 To evaluate the dependence of autoconversion and accretion rates on sub-grid variabilities  
239 for different model spatial resolutions, an averaged wind speed within a cloud layer was  
240 extracted from merged sounding and used in sampling observations over certain periods to  
241 mimic different grid sizes in GCMs. For example, two hours of observations corresponds to a

72-km grid box if mean in-cloud wind speed is  $10 \text{ m s}^{-1}$  horizontal wind and if the wind speed is  $5 \text{ m s}^{-1}$ , four hours of observations is needed to mimic the same grid. We used six grid sizes (30-, 60-, 90-, 120-, 150-, and 180-km) and mainly show the results from 60-km and 180-km grid sizes in Section 4.

## 4. Results and discussions

In this section, we first show the data and methods using a selected case, followed by statistical analysis based on 19 months of data and multiple time-intervals.

### 4.1 Case study

The selected case occurred on July 27, 2010 (Figure 1a) at the Azores. This case was characterized by a long time of non-precipitating or light drizzling cloud development (00:00-14:00 UTC) before intense drizzling occurred (14:00-20:00 UTC). Wu et al. (2017) studied this case in detail to demonstrate the effect of wind shear on drizzle initiation. Here, we choose two periods corresponding to a 180-km grid and having similar mean  $q_c$  near cloud top:  $0.28 \text{ g kg}^{-1}$  for period c and  $0.26 \text{ g kg}^{-1}$  for period d but with different distributions (Figures 1c and 1d). The PDFs of  $q_c$  are then fitted using gamma distributions to get shape parameters ( $\nu$ ) as shown in Figures 1c and 1d. Smaller  $\nu$  is usually associated with a more inhomogeneous cloud field, which allows more rapid drizzle production and more efficient liquid transformation from cloud to rain (Xie and Zhang, 2015) in regions that satisfy precipitation criteria, which is usually controlled using threshold  $q_r$ , droplet size or relative humidity (Kessler, 1969; Liu and

261 Daum, 2004). The period d has a wider  $q_c$  distribution than the period c, resulting in a smaller  
262  $\nu$  and thus larger  $E_{auto}$ . Using the fitted  $\nu$ , the  $E_{auto}$  from  $q_c$  is calculated from Eq. (5) and the  
263 period d is larger than the period c (1.80 vs. 1.33). The  $E_{auto}$  values for the periods d and c can  
264 also be calculated from  $N_c$  using the same procedure as  $q_c$  with a similar result (2.1 vs. 1.51).  
265 The  $E_{accr}$  values for the periods d and c can be calculated from the covariance of  $q_c$  and  $q_r$  and  
266 Eq. (7). Not surprisingly, the period d has larger  $E_{accr}$  than the period c. The combination of  
267 larger  $E_{auto}$  and  $E_{accr}$  in the period d contributes to the rapid drizzle production and high rain  
268 rate as seen from WACR reflectivity and  $q_r$ .

269 It is important to understand the physical meaning of enhancement factors in precipitation  
270 parameterization. For example, if we assume two scenarios for  $q_c$  with a model grid having the  
271 same mean values but different distributions: (1) The distribution is extremely homogeneous,  
272 there will be no sub-grid variability because the cloud has the same chance to precipitate and  
273 the enhancement factors would be unity (this is true for arbitrary grid-mean  $q_c$  amount as well).  
274 (2) The cloud field gets more and more inhomogeneous with a broad range of  $q_c$  within the  
275 model grid box, which results in a greater enhancement factor and increases the possibility of  
276 precipitation. That is, a large enhancement factor can make the part of the cloud with higher  $q_c$   
277 within the grid box become more efficient in generating precipitation, rather than the entire  
278 model grid.

Using the LWP retrieved from the Moderate Resolution Imaging Spectroradiometer (MODIS) as an indicator of cloud inhomogeneous, Wood and Hartmann (2006) found that when clouds become more inhomogeneous, cloud fraction decreases, and open cells become dominant with stronger drizzling process (Comstock et al., 2007). The relationship between reduced homogeneity and stronger precipitation intensity is found in this study, which is similar to the findings in other studies (e.g., Wood and Hartmann, 2006, Comstock et., 2007, Barker et al., 1996; Pincus et al., 1999).

It is clear that  $q_c$  and  $N_c$  in Figure 1b are correlated with each other. In addition to their natural relationships,  $q_c$  and  $N_c$  in our retrieval method are also correlated (Dong et al., 2014a and 2014b). Thus, the effect of  $q_c$  and  $N_c$  covariance on  $E_{auto}$  is not included in this study. In Figures 1c and 1d, the results are calculated using model grid of 180-km for the selected case on 27 July 2010. In Section 4.2, we will use these approaches to calculate their statistical results for multiple grid sizes using the 19-month ARM ground-based observations and retrievals.

## 4.2 Statistical result

For a specific grid size, e.g. 60-km, we estimate the shape parameter ( $\nu$ ) and calculate  $E_{auto}$  through Eqns. (5) and (7). The PDFs of  $E_{auto}$  for both 60-km and 180-km grids are shown in Figures 2a-2d. The distributions of  $E_{auto}$  values calculated from  $q_c$  with 60-km and 180-km grid sizes (Figures 2a and 2b) are different to each other (2.79 vs. 3.3). The calculated  $E_{auto}$  values range from 1 to 10, and most are less than 4. The average value for the 60-km grid (2.79) is



298 smaller than that for the 180-km grid (3.2), indicating a possible dependence of  $E_{auto}$  on model  
 299 grid size. Because drizzle-sized drops are primarily resulted from the autoconversion, we  
 300 investigate the relationship between  $E_{auto}$  and precipitation frequency, which is defined as the  
 301 average percentage of drizzling occurrence based on radar reflectivity below the cloud base.  
 302 Given the average LWP at Azores from Dong et al. (2014b, 109-140 g m<sup>-2</sup>), the precipitation  
 303 frequency (black lines in Figures 2a and 2b) agrees well with those from Kubar et al. (2009,  
 304 0.1-0.7 from their Figure 11). The precipitation frequency within each bin shows an increasing  
 305 trend for  $E_{auto}$  from 0 to 4-6, then oscillates around a relative constant when  $E_{auto} > 6$ , indicating  
 306 that in precipitation initiation process,  $E_{auto}$  keeps increasing to a certain value ( $\sim 6$ ) until the  
 307 precipitation frequency reaches a near-steady state. Larger  $E_{auto}$  values do not necessarily result  
 308 in higher precipitation frequency but instead may produce more drizzle-sized drops from  
 309 autoconversion process when the cloud is precipitating.

310 The PDFs of  $E_{auto}$  calculated from  $N_c$  also share similar patterns of positive skewness and  
 311 peaks at  $\sim 1.5$ -2.0 for the 60-km and 180-km grid sizes (Figures 2c and 2d). Although the  
 312 average values are close to their  $q_c$  counterparts (2.54 vs. 2.79 for 60-km and 3.45 vs. 3.2 for  
 313 180-km), the difference in  $E_{auto}$  between 60-km and 180-km grid sizes becomes large. The  
 314 precipitation frequencies within each bin are nearly constant or slightly decrease, which are  
 315 different to their  $q_c$  counterparts shown in Figures 2a and 2b. This suggests complicated effects  
 316 of droplet number concentration on precipitation initiation and warrants more explorations of

317 aerosol-cloud-precipitation interactions. This is very intriguing result, which suggests the  
 318 existence of significant sub-grid variation of  $N_c$  and this variation can significantly influence  
 319 the warm rain process. As mentioned in Section 2,  $q_c$  and  $N_c$  are also fitted using lognormal  
 320 distributions to calculate  $E_{auto}$ , those are close to the results in Figure 2 (not shown here) with  
 321 average values of 3.28 and 3.84, respectively, for 60-km and 180-km grid sizes. Because the  
 322  $E_{auto}$  values calculated from  $q_c$  and  $N_c$  are close to each other, we will focus on analyzing the  
 323 results from  $q_c$  only for simplicity and clarity. The effect of  $q_c$  and  $N_c$  covariance, as stated in  
 324 Section 4.1, is not presented in this study due to the intrinsic correlation in the retrieval (Dong  
 325 et al., 2014a and 2014b and Appendix A of this study).

326 The covariance of  $q_c$  and  $q_r$  is included in calculating  $E_{accr}$  and the results are shown in  
 327 Figures 2e and 2f. The calculated  $E_{accr}$  values range from 1 to 4 with mean values of 1.62 and  
 328 1.76 for 60-km and 180-km grid sizes, respectively. These two mean values are much greater  
 329 than the prescribed value used in MG08 (1.07). Since accretion is dominant at middle and lower  
 330 parts of the cloud where rain drops sediment and continue to grow by collecting cloud droplets,  
 331 we superimpose the ratio of  $q_r$  to  $q_c$  within each bin (black lines in Figures 2e and 2f) to  
 332 represent the portion of rain water in the cloud layer. In both panels, the ratios are less than  
 333 15%, which means that  $q_r$  can be one order of magnitude smaller than  $q_c$ . The differences in  
 334 magnitude are consistent with previous CloudSat and aircraft results (e.g., Boutle et al., 2014).  
 335 This ratio increases from  $E_{accr}=0$  to  $\sim 2$ , and then decreases, suggesting a possible optimal state

336 for the collision-coalescence process to achieve maximum efficiency for converting cloud  
 337 water into rain water at  $E_{accr}=2$ . In other words, the conversion efficiency cannot be infinitely  
 338 increased with  $E_{accr}$  under available cloud water. The ratio of  $q_r$  to  $q_c$  increases from  $E_{accr}=1.07$   
 339 (0.063) to  $E_{accr}=2.0$  (0.142), indicating that the fraction of rain water in total water using the  
 340 prescribed  $E_{accr}$  is too low. This ratio could be increased significantly using a large  $E_{accr}$  value,  
 341 therefore increasing precipitation intensity in the models. This further proves that the  
 342 prescribed value of  $E_{accr}=1.07$  used in MG08 is too small to correctly simulate precipitation  
 343 intensity in the models. Therefore, similar to the conclusions in Lebsock et al. (2013) and  
 344 Boutle et al. (2014), we suggest increasing  $E_{accr}$  from 1.07 to 1.5-2.0 in GCMs.

345 To illustrate the impact of using prescribed enhancement factors, autoconversion and  
 346 accretion rates are calculated using the prescribed values (e.g., 3.2 for  $E_{auto}$  and 1.07 for  $E_{accr}$ ,  
 347 MG08; Xie and Zhang, 2015) and the newly calculated ones in Figure 2 that use observations  
 348 and retrievals. Figure 3 shows the joint density of autoconversion (Figures 3a and 3b) and  
 349 accretion rates (Figures 3c and 3d) from observations (x-axis) and model parameterizations (y-  
 350 axis) for 60-km and 180-km grid sizes. Despite the spread, the peaks of the joint density of  
 351 autoconversion rate appear slightly above the one-to-one line, suggesting that cloud droplets in  
 352 the model are more easily to be converted into drizzle/rain drops than observations. On the  
 353 other hand, the peaks of accretion rate appear slightly below the one-to-one line which indicates  
 354 that simulated precipitation intensities are lower than observed ones. The magnitudes of the

355 two rates are consistent with Khairoutdinov and Kogan (2000), Liu and Daum (2004), and  
356 Wood (2005b).

357 Compared to the observations, the precipitation in GCMs occurs at higher frequencies with  
358 lower intensities, which might explain why the total precipitation amounts are close to surface  
359 measurements over an entire grid box. This ‘promising’ result, however, fails to simulate  
360 precipitation on the right scale and cannot capture the correct rain water amount, thus providing  
361 limited information in estimating rain water evaporation and air-sea energy exchange.

362 Clouds in an unstable boundary layer have a better chance of getting moisture supply from  
363 the surface by upward motion than clouds in a stable boundary layer. Precipitation frequencies  
364 are thus different in these two boundary layer regimes. For example, clouds in a relatively  
365 unstable boundary layer more easily produce drizzle than those in a stable boundary layer (Wu  
366 et al., 2017). Provided the same boundary layer condition, CLWP is an important factor in  
367 determining the precipitation status of clouds. At the Azores, precipitating clouds are more  
368 likely to have CLWP greater than  $75 \text{ g m}^{-2}$  than their nonprecipitating counterparts (Rémillard  
369 et al., 2012). To further investigate what conditions and parameters can significantly influence  
370 the enhancement factors, we classify low-level clouds according to their boundary layer  
371 conditions and CLWPs.

372 The averaged  $E_{auto}$  and  $E_{accr}$  values for each category are listed in Table 2. Both  $E_{auto}$  and  
373  $E_{accr}$  increase when the boundary layer becomes less stable, and these values become larger in

precipitating clouds ( $CLWP > 75 \text{ gm}^{-2}$ ) than those in nonprecipitating clouds ( $CLWP < 75 \text{ gm}^{-2}$ ). In real applications, autoconversion process only occurs when  $q_c$  or cloud droplet size reaches a certain threshold (e.g., Kessler, 1969 and Liu and Daum, 2004). Thus, it will not affect model simulations if a valid  $E_{auto}$  is assigned to Eq. (1) in a nonprecipitating cloud. The  $E_{auto}$  values in both stable and mid-stable boundary layer conditions are smaller than the prescribed value of 3.2, while the values in unstable boundary layers are significantly larger than 3.2 regardless of if they are precipitating or not. All  $E_{accr}$  values are greater than the constant of 1.07. The  $E_{auto}$  values in Table 2 range from 2.32 to 6.94 and the  $E_{accr}$  values vary from 1.42 to 1.86, depending on different boundary layer conditions and CLWPs. Therefore, as suggested by Hill et al. (2015), the selection of  $E_{auto}$  and  $E_{accr}$  values in GCMs should be regime-dependent.

To properly parameterize sub-grid variabilities, the approaches by Hill et al. (2015) and Walters et al. (2017) can be adopted. To use MG08 and other parameterizations in GCMs as listed in Table 1, proper adjustments can be made according to the model grid size, boundary layer conditions, and precipitating status. As stated in the methodology, we used a variety of model grid sizes. Figure 4 demonstrates the dependence of both enhancement factors on different model grid sizes. The  $E_{auto}$  values (red line) increase from 1.97 at a grid box of  $30 \times 30$  km to 3.15 at a grid box of  $120 \times 120$  km, which are 38.4% and 2% percent lower than the prescribed value (3.2, upper dashed line). After that, the  $E_{auto}$  values remain relatively constant of  $\sim 3.18$  when the model grid is 180 km, which is close to the prescribed value of 3.2 used in

MG08. This result indicates that the prescribed value in MG08 represents well in large grid sizes in GCMs. The  $E_{accr}$  values (blue line) increase from 1.53 at a grid box of 30×30 km to 1.76 at a grid box of 180×180 km, those are 43% and 64%, respectively, larger than the prescribed value (1.07, lower dashed line). The shaded areas represent the uncertainties of  $E_{auto}$  and  $E_{accr}$  associated with the uncertainties of the retrieved  $q_c$  and  $q_r$ . When model grid size increases, the uncertainties slightly decrease. The prescribed  $E_{auto}$  is close to the upper boundary of uncertainties except for the 30-km grid size, while the prescribed  $E_{accr}$  is significantly lower than the lower boundary.

It is noted that  $E_{auto}$  and  $E_{accr}$  depart from their prescribed values at opposite directions as model grid size increases. For models with finer resolutions (e.g., 30-km), both  $E_{auto}$  and  $E_{accr}$  are significantly different from the prescribed values, which can partially explain the issue of ‘too frequent’ and ‘too light’ precipitation. Under both conditions, the accuracy of precipitation estimation is degraded. For models with coarser resolutions (e.g., 180-km), average  $E_{auto}$  is exactly 3.2 while  $E_{accr}$  is much larger than 1.07 when compared to finer resolution simulations. In such situations, the simulated precipitation will be dominated by the ‘too light’ problem, in addition to regime-dependent (Table 2) and as in Xie and Zhang (2015),  $E_{auto}$  and  $E_{accr}$  should be also scale-dependent.

Also note that the location we choose to collect ground-based observations and retrievals is on the remote ocean where the MBL clouds mainly form in a relatively stable boundary layer

412 and are characterized by high precipitation frequency. Even in such environments, however,  
413 the GCMs overestimate the precipitation frequency (Ahlgrimm and Forbes, 2014).

414 To further investigate how enhancement factors affect precipitation simulations, we use  
415  $E_{auto}$  as a fixed value of 3.2 in Eq. (4), and then calculate the  $q_c$  needed for models to reach the  
416 same autoconversion rate as observations. The  $q_c$  differences between models and observations  
417 are then calculated, which represent the  $q_c$  adjustment in models to get a realistic  
418 autoconversion rate in the simulations. Similar to Figure 1, the PDFs of  $q_c$  differences (model  
419 – observation) are plotted in Figures 5a and 5b for 60-km and 180-km grid sizes. Figure 5c  
420 shows the average percentages of model  $q_c$  adjustments for different model grid sizes. The  
421 mode and average values for 30-km grid is negative, suggesting that models need to simulate  
422 lower  $q_c$  in general to get reasonable autoconversion rates. Lower  $q_c$  values are usually  
423 associated with smaller  $E_{auto}$  values that induce lower simulated precipitation frequency. On  
424 average, the percentage of  $q_c$  adjustments decrease with increasing model grid size. For  
425 example, the adjustments for finer resolutions (e.g., 30-60 km) can be ~20% of the  $q_c$ , whereas  
426 adjustments in coarse resolution models (e.g., 120 – 180 km) are relatively small because the  
427 prescribed  $E_{auto}$  (=3.2) is close to the observed ones (Figure 4) and when model grid size is  
428 180-km, no adjustment is needed. The adjustment method presented in Figure 5, however, may  
429 change cloud water substantially and may cause a variety of subsequent issues, such as altering  
430 cloud radiative effects and disrupting the hydrological cycle. The assessment in Figure 5 only

431 provides a reference to the equivalent effect on cloud water by using the prescribed  $E_{auto}$  value  
432 as compared to those from observations.

433 All above discussions are based on the prescribed  $E_{auto}$  and  $E_{accr}$  values (3.2 and 1.07) in  
434 MG08. Whereas there are quite a few parameterizations that have been published so far. In this  
435 study, we list  $E_{auto}$  and  $E_{accr}$  for three other widely used parameterization schemes in Table 3,  
436 which are given only for 60-km and 180-km grid sizes. The values of the exponent in each  
437 scheme directly affect the values of the enhancement factors. For example, the scheme in  
438 Beheng (1994) has highest degree of nonlinearity and hence has the largest enhancement  
439 factors. The scheme in Liu and Daum (2004) is very similar to the scheme in Khairoutdinov  
440 and Kogan (2000) because both schemes have a physically realistic dependence on cloud water  
441 content and number concentration (Wood, 2005b). For a detailed overview and discussion of  
442 various existing parameterizations, please refer to Liu and Daum (2004), Liu et al. (2006a), Liu  
443 et al. (2004b), Wood (2005b) and Michibata and Takemura (2015). A physical based  
444 autoconversion parameterization was developed by Lee and Baik (2017) in which the scheme  
445 was derived by solving stochastic collection equation with an approximated collection kernel  
446 that is constructed using the terminal velocity of cloud droplets and the collision efficiency  
447 obtained from a particle trajectory model. Due to the greatly increased complexity of their  
448 equation, we do not attempt to calculate  $E_{auto}$  here but should be examined in future studies due  
449 to the physics feasibility of the Lee and Baik (2017) scheme.



450

## 451 **5. Summary**

452 To better understand the influence of sub-grid cloud variations on the warm-rain process  
453 simulations in GCMs, we investigated the warm-rain parameterizations of autoconversion  
454 ( $E_{auto}$ ) and accretion ( $E_{accr}$ ) enhancement factors in MG08. These two factors represent the  
455 effects of sub-grid cloud and precipitation variabilities when parameterizing autoconversion  
456 and accretion rates as functions of grid-mean quantities.  $E_{auto}$  and  $E_{accr}$  are prescribed as 3.2  
457 and 1.07, respectively, in the widely used MG08 scheme. To assess the dependence of the two  
458 parameters on sub-grid scale variabilities, we used ground-based observations and retrievals  
459 collected at the DOE ARM Azores site to reconstruct the two enhancement factors in different  
460 model grid sizes.

461 From the retrieved  $q_c$  and  $q_r$  profiles, the averaged  $q_c$  within the top five range gates are  
462 used to calculate  $E_{auto}$  and the averaged  $q_c$  and  $q_r$  within five range gates around maximum  
463 reflectivity are used to calculate  $E_{accr}$ . The calculated  $E_{auto}$  values from observations and  
464 retrievals increase from 1.96 at a grid box of 30×30 km to 3.15 at a grid box of 120×120 km.  
465 These values are 38% and 2% lower than the prescribed value of 3.2. The prescribed value in  
466 MG08 represents well in large grid sizes in GCMs. On the other hand, the  $E_{accr}$  values increase  
467 from 1.53 at a grid box of 30×30 km to 1.76 at a grid box of 180×180 km, which are 43% and  
468 64% higher than the prescribed value (1.07). The higher  $E_{auto}$  and lower  $E_{accr}$  prescribed in

469 GCMs help to explain the issue of too frequent precipitation events with too light precipitation  
470 intensity. The ratios of rain to cloud liquid water increase with increasing  $E_{accr}$  from 0 to 2, and  
471 then decrease after that, suggesting a possible optimal state for the collision-coalescence  
472 process to achieve maximum efficiency for converting cloud water into rain water at  $E_{accr}=2$ .  
473 The ratios of  $q_r$  to  $q_c$  at  $E_{accr}=1.07$  and  $E_{accr}=2.0$  are 0.063 and 0.142, further proving that the  
474 prescribed value of  $E_{accr}=1.07$  is too small to simulate correct precipitation intensity in models.

475 To further investigate what conditions and parameters can significantly influence the  
476 enhancement factors, we classified low-level clouds according to their boundary layer  
477 conditions and CLWPs. Both  $E_{auto}$  and  $E_{accr}$  increase when the boundary layer conditions  
478 become less stable, and the values are larger in precipitating clouds ( $CLWP > 75 \text{ gm}^{-2}$ ) than  
479 those in nonprecipitating clouds ( $CLWP < 75 \text{ gm}^{-2}$ ). The  $E_{auto}$  values in both stable and mid-stable  
480 boundary layer conditions are smaller than the prescribed value of 3.2, while those in unstable  
481 boundary layers conditions are significantly larger than 3.2 regardless of whether or not the  
482 cloud is precipitating (Table 2). All  $E_{accr}$  values are greater than the prescribed value of 1.07.  
483 Therefore, the selection of  $E_{auto}$  and  $E_{accr}$  values in GCMs should be regime-dependent, which  
484 also has been suggested by Hill et al. (2015) and Walters et al. (2017).

485 This study, however, did not include the effect of uncertainties in GCM simulated cloud  
486 and precipitation properties on sub-grid scale variations. For example, we did not consider the  
487 behavior of the two enhancement factors under different aerosol regimes, a condition which

may affect precipitation formation process. The effect of aerosol-cloud-precipitation- interactions on cloud and precipitation sub-grid variabilities may be of comparable importance to meteorological regimes and precipitation status and deserves a further study. Other than the large-scale dynamics, e.g., LTS in this study, upward/downward motion in sub-grid scale may also modify cloud and precipitation development and affect the calculations of enhancement factors. The investigation of the dependence of  $E_{auto}$  and  $E_{accr}$  on aerosol type and concentration as well as on vertical velocity would be a natural extension and complement of current study. In addition, other factors may also affect precipitation frequency and intensity even under the same aerosol regimes and even if the clouds have similar cloud water contents. Wind shear, for example as presented in Wu et al. (2017), is an external variable that can affect precipitation formation. Further studies are needed to evaluate the role of the covariance of  $q_c$  and  $N_c$  in sub-grid scales on  $E_{auto}$  determinations, which is beyond the scope of this study and requires independent retrieval techniques.

501

## 502 **Appendix A: Joint cloud and rain LWC profile estimation**

503 If a time step is identified as non-precipitating, the cloud liquid water content (CLWC)  
504 profile is retrieved using Frisch et al. (1995) and Dong et al. (1998, 2014a and 2014b). The  
505 retrieved CLWC is proportional to radar reflectivity.

506 If a time step is identified as precipitating (maximum reflectivity below cloud base  
 507 exceeds -37 dBZ), CLWC profile is first inferred from temperature and pressure in merged  
 508 sounding by assuming adiabatic growth. Marine stratocumulus is close to adiabatic (Albrecht  
 509 et al. 1990) and was used in cloud property retrievals in literature (e.g., Rémillard et al., 2013).  
 510 In this study, we use the information from rain properties near cloud base to further constrain  
 511 the adiabatic CLWC ( $CLWC_{adiabatic}$ ).

512 Adopting the method of O'Connor et al. (2005), Wu et al. (2015) retrieved rain properties  
 513 below cloud base (CB) for the same period as in this study. In Wu et al. (2015), rain drop size  
 514 (median diameter,  $D_0$ ), shape parameter ( $\mu$ ), and normalized rain droplet number concentration  
 515 ( $N_W$ ) are retrieved for the assumed rain particle size distribution (PSD):

$$516 \quad n_r(D) = N_W f(\mu) \left(\frac{D}{D_0}\right)^\mu \exp\left[-\frac{(3.67+\mu)D}{D_0}\right] \quad (A1)$$

517 To infer rain properties above cloud base, we adopt the assumption in Fielding et al. (2015)  
 518 that  $N_W$  increases from below CB to within the cloud. This assumption is consistent with the *in*  
 519 *situ* measurement in Wood (2005a). Similar as Fielding et al. (2015), we use constant  $N_W$  within  
 520 cloud if the  $N_W$  decrease with height below CB. The  $\mu$  within cloud is treated as constant and  
 521 is taken as the averaged value from four range gates below CB. Another assumption in the  
 522 retrieval is that the evaporation of rain drops is negligible from one range gate above CB to one  
 523 range gate below CB thus we assume rain drop size is the same at the range gate below and  
 524 above CB.

525 With the above information, we can calculate the reflectivity contributed by rain at the first  
 526 range gate above CB ( $Z_d(1)$ ) and the cloud reflectivity ( $Z_c(1)$ ) is then  $Z_c(1) = Z(1) - Z_d(1)$ ,  
 527 where  $Z(1)$  is WACR measured reflectivity at first range gate above CB. Using cloud droplet  
 528 number concentration ( $N_c$ ) from Dong et al. (2014a and 2014b), CLWC at the first range gate  
 529 above CB can be calculated through

$$530 \quad Z_c(1) = 2^6 \int_0^\infty n_c(r) r^6 dr = \frac{36}{\pi^2 \rho_w^2} \frac{CLWC(1)_{reflectivity}^2}{N_c} \exp(9\sigma_x^2) \quad (A2)$$

531 where  $n_c(r)$  is lognormal distribution of cloud PSD with logarithmic width  $\sigma_x$  which is set to  
 532 a constant value of 0.38 (Miles et al., 2000),  $\rho_w$  is liquid water density.

533 We then compare the  $CLWC_{adiabatic}$  and the one calculated from  $CLWC_{reflectivity}$  at the  
 534 first range gate above CB. A scale parameter ( $s$ ) is defined as  $s = \frac{CLWC_{reflectivity}(1)}{CLWC_{adiabatic}(1)}$  and the  
 535 entire profile of  $CLWC_{adiabatic}$  is multiplied by  $s$  to correct the bias from cloud sub-  
 536 adiabaticity. Reflectivity profile from cloud is then calculated from Eq. (A2) and the remaining  
 537 reflectivity profile from WACR observation is regarded as rain contribution. Rain particle size  
 538 can then be calculated given that  $N_w$  and  $\mu$  are known and rain liquid water content (RLWC)  
 539 can be estimated.

540 There are two constraints used in the retrieval. One is that the summation of cloud and rain  
 541 liquid water path (CLWP and RLWP) must be equal to the LWP from microwave radiometer  
 542 observation. Another is that rain drop size ( $D_0$ ) near cloud top must be equal or greater than 50

543  $\mu m$  and if  $D_0$  is less than  $50 \mu m$ , we decrease  $N_W$  for the entire rain profile within cloud and  
544 repeat the calculation until the  $50 \mu m$  criteria is satisfied.

545 It is difficult to quantitatively estimate the retrieval uncertainties without aircraft in situ  
546 measurements. For the proposed retrieval method, 18% should be used as uncertainty for  
547 RLWC from rain properties in Wu et al. (2015) and 30% for CLWC from cloud properties in  
548 Dong et al. (2014a and 2014b). The actual uncertainty depends on the accuracy of merged  
549 sounding data, the detectability of WACR near cloud base and the effect of entrainment on  
550 cloud adiabaticity during precipitating. In the recent aircraft field campaign, the Aerosol and  
551 Cloud Experiments in Eastern North Atlantic (ACE-ENA) was conducted during 2017-2018  
552 with a total of 39 flights over the Azores, near the ARM ENA site on Graciosa Island. These  
553 aircraft in situ measurements will be used to validate the ground-based retrievals and  
554 quantitatively estimate their uncertainties in the future.

555 Figure A1 shows an example of the retrieval results. The merged sounding, ceilometer,  
556 microwave radiometer, WACR and ceilometer are used in the retrieval. Whenever one or more  
557 instruments are not reliable, that time step is skipped, and this results in the gaps in the CLWC  
558 and RLWC as shown in Figures A1(b) and A1(c). When the cloud is classified as  
559 nonprecipitating, no RLWC will be retrieved as well. Using air density ( $\rho_{air}$ ) profiles  
560 calculated from temperature and pressure in merged sounding, mixing ratio ( $q$ ) can be  
561 calculated from LWC using  $q(z) = LWC(z)/\rho_{air}(z)$ .

## 562 **Acknowledgements**

563 The ground-based measurements were obtained from the Atmospheric Radiation Measurement  
564 (ARM) Program sponsored by the U.S. Department of Energy (DOE) Office of Energy  
565 Research, Office of Health and Environmental Research, and Environmental Sciences  
566 Division. The data can be downloaded from <http://www.archive.arm.gov/>. This research was  
567 supported by the DOE CESM project under grant DE-SC0014641 at the University of Arizona  
568 through subaward from University of Maryland at Baltimore County, and the NSF project  
569 under grant AGS-1700728 at University of Arizona. The authors thank Dr. Yangang Liu at  
570 Brookhaven National Laboratory for insightful comments and Ms. Casey E. Oswant at the  
571 University of Arizona for proof reading the manuscript. The two anonymous reviewers are  
572 acknowledged for constructive comments and suggestions which helped to improve the  
573 manuscript.

574

## 575 **References**

576 Ackerman, A. S., Kirkpatrick, M. P., Stevens, D. E., and Toon, O. B.: The impact of humidity  
577 above stratiform clouds on indirect aerosol climate forcing, *Nature*, 432, 1014–1017, 2004.  
578 Ahlgrimm, M., and Forbes, R.: Improving the Representation of Low Clouds and Drizzle in  
579 the ECMWF Model Based on ARM Observations from the Azores, *J. Clim.*, doi:  
580 10.1175/MWR-D-13-00153.1, 2014.  
581 Albrecht, B. A.: Aerosols, cloud microphysics, and fractional cloudiness, *Science*, 245, 1227–  
582 1231, 1989.

583 Albrecht, B., Fairall, C., Thomson, D., White, A., Snider, J., and Schubert, W.: Surface-based  
 584 remote-sensing of the observed and the adiabatic liquid water-content of stratocumulus  
 585 clouds, *Geophys. Res. Lett.*, 17, 89–92, doi:10.1029/G1017i001p00089, 1990.  
 586 Austin, P., Wang, Y., Kujala, V., and Pincus, R.: Precipitation in Stratocumulus Clouds:  
 587 Observational and Modeling Results, *J. Atmos. Sci.*, 52, 2329–2352, doi:10.1175/1520-  
 588 0469(1995)052<2329:PISCOA>2.0.CO;2, 1995.  
 589 Bai, H., Gong, C., Wang, M., Zhang, Z., and L'Ecuyer, T.: Estimating precipitation  
 590 susceptibility in warm marine clouds using multi-sensor aerosol and cloud products from  
 591 A-Train satellites, *Atmos. Chem. Phys.*, 18, 1763-1783, [https://doi.org/10.5194/acp-18-](https://doi.org/10.5194/acp-18-1763-2018)  
 592 1763-2018, 2018.  
 593 Barker H. W., Wiellicki B.A., Parker L.: A parameterization for computing grid-averaged solar  
 594 fluxes for inhomogeneous marine boundary layer clouds. Part II: Validation using satellite  
 595 data. *J. Atmos. Sci.* 53: 2304–2316, 1996.  
 596 Beheng, K. D.: A parameterization of warm cloud microphysical conversion processes, *Atmos.*  
 597 *Res.*, 33, 193-206, 1994.  
 598 Bony, S., and Dufresne, J.-L.: Marine boundary layer clouds at the heart of tropical cloud  
 599 feedback uncertainties in climate models, *Geophys. Res. Lett.*, 32, L20806,  
 600 doi:10.1029/2005GL023851, 2005.  
 601 Boutle, I. A., Abel, S. J., Hill, P. G., and Morcrette, C. J.: Spatial variability of liquid cloud and  
 602 rain: Observations and microphysical effects. *Quart. J. Roy. Meteor. Soc.*, 140, 583–594,  
 603 doi:10.1002/qj.2140, 2014.  
 604 Chen, T., Rossow, W. B., and Zhang, Y.: Radiative Effects of Cloud-Type Variations, *J. Clim.*,  
 605 13, 264–286, 2000.  
 606 Cheng, A., and Xu. K.-M.: A PDF-based microphysics parameterization for simulation of  
 607 drizzling boundary layer clouds, *J. Atmos. Sci.*, 66, 2317–2334,  
 608 doi:10.1175/2009JAS2944.1, 2009.



609 Comstock, K. K., Yuter, S. E., Wood, R., and Bretherton, C. S.: The Three-Dimensional  
610 Structure and Kinematics of Drizzling Stratocumulus, *Mon. Weather Rev.*, 135, 3767–  
611 3784, doi:10.1175/2007MWR1944.1, 2007.

612 Dong X., Ackerman, T. P., and Clothiaux, E. E.: Parameterizations of Microphysical and  
613 Radiative Properties of Boundary Layer Stratus from Ground-based measurements, *J.*  
614 *Geophys. Res.*, 102, 31,681-31,393, 1998.

615 Dong, X., Minnis, P., Ackerman, T. P., Clothiaux, E. E., Mace, G. G., Long, C. N., and  
616 Liljegren, J. C.: A 25-month database of stratus cloud properties generated from ground-  
617 based measurements at the ARM SGP site, *J. Geophys. Res.*, 105, 4529-4538, 2000.

618 Dong, X., Xi, B., Kennedy, A., Minnis, P. and Wood, R.: A 19-month Marine Aerosol-  
619 Cloud\_Radiation Properties derived from DOE ARM AMF deployment at the Azores:  
620 Part I: Cloud Fraction and Single-layered MBL cloud Properties, *J. Clim.*, 27,  
621 doi:10.1175/JCLI-D-13-00553.1, 2014a.

622 Dong, X., Xi, B., and Wu, P.: Investigation of Diurnal Variation of MBL Cloud Microphysical  
623 Properties at the Azores, *J. Clim.*, 27, 8827-8835, 2014b.

624 Fielding, M. D., Chiu, J. C., Hogan, R. J., Feingold, G., Eloranta, E., O'Connor, E. J. and  
625 Cadeddu, M. P.: Joint retrievals of cloud and drizzle in marine boundary layer clouds using  
626 ground-based radar, lidar and zenith radiances. *Atmospheric Measurement Techniques*, 8.  
627 pp. 2663-2683. ISSN 1867-8548 doi: 10.5194/amt-8-2663-2015, 2015.

628 Frisch, A., Fairall, C., and Snider, J.: Measurement of stratus cloud and drizzle parameters in  
629 ASTEX with a Ka-band Doppler radar and a microwave radiometer, *J. Atmos. Sci.*, 52,  
630 2788–2799, 1995.

631 Hahn, C. and Warren, S.: A gridded climatology of clouds over land (1971–96) and ocean  
632 (1954–97) from surface observations worldwide, *Numeric Data Package NDP-026E*  
633 *ORNL/CDIAC-153*, CDIAC, Department of Energy, Oak Ridge, Tennessee, 2007.

634 Hartmann, D. L., Ockert-Bell, M. E., and Michelsen, M. L.: The Effect of Cloud Type on  
635 Earth's Energy Balance: Global Analysis, *J. Climate*, 5, 1281–1304,  
636 [https://doi.org/10.1175/15200442\(1992\)005<1281:TEOCTO>2.0.CO;2](https://doi.org/10.1175/15200442(1992)005<1281:TEOCTO>2.0.CO;2), 1992.

637 Hartmann, D. L. and Short, D. A.: On the use of earth radiation budget statistics for studies of  
638 clouds and climate, *J. Atmos. Sci.*, 37, 1233–1250, doi:10.1175/1520-  
639 0469(1980)037<1233:OTUOER>2.0.CO;2, 1980.

640 Hill, P. G., Morcrette, C. J., and Boutle, I. A.: A regime-dependent parametrization of subgrid-  
641 scale cloud water content variability, *Q. J. R. Meteorol. Soc.*, 141, 1975–1986, 2015.

642 Houghton, J. T., Ding, Y., Griggs, D.J., Noguer, M., van der Linden, P.J., Dai, X., Maskell, K.,  
643 and Johnson, C.A.: *Climate Change: The Scientific Basis*, Cambridge University Press,  
644 881 pp, 2001.

645 Jess, S.: Impact of subgrid variability on large-scale precipitation formation in the climate  
646 model ECHAM5, PhD thesis, Dep. of Environ. Syst. Sci., ETH Zurich, Zurich,  
647 Switzerland, 2010.

648 Jiang, J., Su, H., Zhai, C., Perun, V. S., Del Genio, A., Nazarenko, L. S., Donner, L. J.,  
649 Horowitz, Seman, L., Cole, C., J., Gettelman, A., Ringer, M. A., Rotstayn, L., Jeffrey, S.,  
650 Wu, T., Brient, F., Dufresne, J-L., Kawai, H., Koshiro, T., Watanabe, M., LÉcuyer, T. S.,  
651 Volodin, E. M., Iversen, Drange, T., H., Mesquita, M. D. S., Read, W. G., Waters, J. W.,  
652 Tian, B., Teixeira, J., and Stephens, G. L.: Evaluation of cloud and water vapor simulations  
653 in CMIP5 climate models using NASA “A-train” satellite observations, *J. Geophys. Res.*,  
654 117, D14105, doi:10.1029/2011JD017237, 2012.

655 Kessler, E.: On the distribution and continuity of water substance in atmospheric circulations,  
656 *Met. Monograph* 10, No. 32, American Meteorological Society, Boston, USA, 84 pp.,  
657 1969.

658 Khairoutdinov, M. and Kogan, Y.: A New Cloud Physics Parameterization in a Large-Eddy  
659 Simulation Model of Marine Stratocumulus, *Mon. Wea. Rev.*, 128, 229–243, 2000.

660 Kooperman, G. J., Pritchard, M. S., Ghan, S. J., Wang, M., Somerville, R. C., and Russell, L.  
 661 M.: Constraining the influence of natural variability to improve estimates of global aerosol  
 662 indirect effects in a nudged version of the Community Atmosphere Model 5, *J. Geophys.*  
 663 *Res.*, 117, D23204, <https://doi.org/10.1029/2012JD018588>, 2012.

664 Kubar, T. L., Hartmann, D. L., and Wood, R.: Understanding the importance of microphysics  
 665 and macrophysics in marine low clouds, Part I: satellite observations. *J. Atmos. Sci.*, 66,  
 666 2953-2972, doi: 10.1175/2009JAS3071.1, 2009.

667 Larson, V. E., Nielsen, B. J., Fan, J., and Ovchinnikov, M.: Parameterizing correlations  
 668 between hydrometeor species in mixed-phase Arctic clouds, *J. Geophys. Res.*, 116,  
 669 D00T02, doi:10.1029/2010JD015570, 2011.

670 Larson, V. E., and Griffin, B. M.: Analytic upscaling of a local microphysics scheme. Part I:  
 671 Derivation. *Quart. J. Roy. Meteor. Soc.*, 139, 46–57, 2013.

672 Lebsock, M. D., Morrison, H., and Gettelman, A.: Microphysical implications of cloud-  
 673 precipitation covariance derived from satellite remote sensing, *J. Geophys. Res.-Atmos.*,  
 674 118, 6521–6533, <https://doi.org/10.1002/jgrd.50347>, 2013.

675 Lee, H., and Baik, J.-J.: A physically based autoconversion parameterization. *Journal of the*  
 676 *Atmospheric Sciences*, 74, 1599–1616, 2017.

677 Leon, D. C., Wang, Z., and Liu, D.: Climatology of drizzle in marine boundary layer clouds  
 678 based on 1 year of data from CloudSat and Cloud-Aerosol Lidar and Infrared Pathfinder  
 679 Satellite Observations (CALIPSO), *J. Geophys. Res.*, 113, D00A14,  
 680 doi:10.1029/2008JD009835, 2008.

681 Liljegren, J. C., Clothiaux, E. E., Mace, G. G., Kato, S., and Dong, X.: A new retrieval for  
 682 cloud liquid water path using a ground-based microwave radiometer and measurements of  
 683 cloud temperature, *J. Geophys. Res.*, 106, 14,485-14,500, 2001.

684 Liu, Y. and Daum, P. H.: Parameterization of the autoconversion process, Part I: Analytical  
 685 formulation of the Kessler-type parameterizations, *J. Atmos. Sci.*, 61, 1539–1548, 2004.

686 Liu, Y., Daum, P. H., and McGraw, R.: Parameterization of the autoconversion process. Part  
 687 II: Generalization of Sundqvist-type parameterizations, *J. Atmos. Sci.*, 63, 1103–1109,  
 688 2006a.

689 Liu, Y., Daum, P. H., McGraw, R., Miller, M.: Generalized threshold function accounting for  
 690 effect of relative dispersion on threshold behavior of autoconversion process. *Geophys.*  
 691 *Res. Lett.*, 33, L11804, 2006b.

692 Lohmann, U. and Feichter, J.: Global indirect aerosol effects: a review, *Atmos. Chem. Phys.*,  
 693 5, 715–737, doi:10.5194/acp-5-715-2005, 2005.

694 Michibata, T., and Takemura, T.: Evaluation of autoconversion schemes in a single model  
 695 framework with satellite observations, *J. Geophys. Res. Atmos.*, 120, 9570–9590,  
 696 doi:10.1002/2015JD023818, 2015.

697 Miles, N. L., Verlinde, J., and Clothiaux, E. E.: Cloud-droplet size distributions in low-level  
 698 stratiform clouds. *J. Atmos. Sci.*, 57, 295–311, doi:10.1175/1520-0469(2000)057,  
 699 0295:CDS DIL.2.0.CO;2, 2000.

700 Morrison, H. and Gettelman, A.: A new two-moment bulk stratiform cloud microphysics  
 701 scheme in the Community Atmosphere Model, version 3 (CAM3). Part I: Description and  
 702 numerical tests, *J. Climate*, 21, 3642–3659, 2008.

703 Nam, C., and Quaas, J.: Evaluation of clouds and precipitation in the ECHAM5 general  
 704 circulation model using CALIPSO and CloudSat satellite data, *J. Clim.*, 25, 4975–4992,  
 705 doi:10.1175/JCLI-D-11-00347.1, 2012.

706 O’Connor, E. J., Hogan, R. J., and Illingworth, A. J.: Retrieving stratocumulus drizzle  
 707 parameters using Doppler radar and lidar, *J. of Applied Meteorol.*, 44, 14-27, 2005.

708 Pincus, R., McFarlane, S. A., and Klein, S. A.: Albedo bias and the horizontal variability of  
 709 clouds in subtropical marine boundary layers: Observations from ships and satellites, *J.*  
 710 *Geophys. Res.*, 104, 6183–6191, doi:10.1029/1998JD200125, 1999.

711 Pincus, R., and Klein, S. A.: Unresolved spatial variability and microphysical process rates in  
712 large-scale models. *J. Geophys. Res.*, 105D, 27 059–27 065, 2000.

713 Quaas, J., Ming, Y., Menon, S., Takemura, T., Wang, M., Penner, J. E., Gettelman, A.,  
714 Lohmann, U., Bellouin, N., Boucher, O., Sayer, A. M., Thomas, G. E., McComiskey, A.,  
715 Feingold, G., Hoose, C., Kristjánsson, J. E., Liu, X., Balkanski, Y., Donner, L. J., Ginoux,  
716 P. A., Stier, P., Grandey, B., Feichter, J., Sednev, Bauer, S. E., Koch, D., Grainger, R. G.,  
717 Kirkevåg, A., Iversen, T., Seland, Ø., Easter, R., Ghan, S. J., Rasch, P. J., Morrison, H.,  
718 Lamarque, J.-F., Iacono, M. J., Kinne, S., and Schulz, M.: Aerosol indirect effects –  
719 general circulation model intercomparison and evaluation with satellite data, *Atmos.*  
720 *Chem. Phys.*, 9, 8697–8717, <https://doi.org/10.5194/acp-9-8697-2009>, 2009.

721 Randall, D. A., Coakley, J. A., Fairall, C. W., Knopfli, R. A., and Lenschow, D. H.: Outlook  
722 for research on marine subtropical stratocumulus clouds. *Bull. Amer. Meteor. Soc.*, 65,  
723 1290–1301, 1984.

724 Rémillard, J., Kollias, P., Luke, E., and Wood, R.: Marine Boundary Layer Cloud Observations  
725 in the Azores, *J. Climate*, 25, 7381–7398, doi: [http://dx.doi.org/10.1175/JCLI-D-11-](http://dx.doi.org/10.1175/JCLI-D-11-00610.1)  
726 00610.1, 2012.

727 Rémillard, J., Kollias, P., and Szyrmer, W.: Radar-radiometer re- trievals of cloud number  
728 concentration and dispersion parameter in nondrizzling marine stratocumulus, *Atmos.*  
729 *Meas. Tech.*, 6, 1817–1828, doi:10.5194/amt-6-1817-2013, 2013.

730 Slingo, A.: Sensitivity of the Earth’s radiation budget to changes in low clouds, *Nature*, 343,  
731 49–51, <https://doi.org/10.1038/343049a0>, 1990.

732 Song, H., Zhang, Z., Ma, P.-L., Ghan, S. J., and Wang, M.: An Evaluation of Marine Boundary  
733 Layer Cloud Property Simulations in the Community Atmosphere Model Using Satellite  
734 Observations: Conventional Subgrid Parameterization versus CLUBB, *J. Clim.*,  
735 doi:10.1175/JCLI-D-17-0277.1, 2018.

736 Stanfield, R., Dong, X., Xi, B., Gel Genio, A., Minnis, P., and Jiang, J.: Assessment of NASA  
 737 GISS CMIP5 and post CMIP5 Simulated Clouds and TOA Radiation Budgets Using  
 738 Satellite Observations: Part I: Cloud Fraction and Properties, *J. Clim.*, doi:10.1175/JCLI-  
 739 D-13-00588.1, 2014.

740 Tripoli, G. J. and Cotton, W. R.: A numerical investigation of several factors contributing to  
 741 the observed variable intensity of deep convection over South Florida., *J. Appl. Meteorol.*,  
 742 19, 1037–1063, 1980.

743 Troyan, D.: Merged Sounding Value-Added Product, Tech. Rep., DOE/SC-ARM/TR-087,  
 744 2012.

745 Walters, D., Baran, A., Boutle, I., Brooks, M., Earnshaw, P., Edwards, J., Furtado, K., Hill, P.,  
 746 Lock, A., Manners, J., Morcrette, C., Mulcahy, J., Sanchez, C., Smith, C., Stratton, R.,  
 747 Tennant, W., Tomassini, L., van Weverberg, K., Vosper, S., Willett, M., Browse, J.,  
 748 Bushell, A., Dalvi, M., Essery, R., Gedney, N., Hardiman, S., Johnson, B., Johnson, C.,  
 749 Jones, A., Mann, G., Milton, S., Rumbold, H., Sellar, A., Ujiie, M., Whittall, M., Williams,  
 750 K. and Zerroukat, M. The Met Office Unified Model Global Atmosphere 7.0/7.1 and  
 751 JULES Global Land 7.0 configurations. *Geosci. Model Dev.*, doi:10.5194/gmd-2017-291,  
 752 2017.

753 Wang, M., Ghan, S., Liu, X., L’Ecuyer, T. S., Zhang, K., Morrison, H., Ovchinnikov, M.,  
 754 Easter, R., Marchand, R., Chand, D., Qian, Y., and Penner, J. E.: Constraining cloud  
 755 lifetime effects of aerosols using A-Train satellite observations, *Geophys. Res. Lett.*, 39,  
 756 L15709, <https://doi.org/10.1029/2012GL052204>, 2012.

757 Warren, S. G., Hahn, C. J., London, J., Chervin, R. M., and Jenne, R.: Global distribution of  
 758 total cloud cover and cloud type amount over land, Tech. Rep. Tech. Note TN-317 STR,  
 759 NCAR, 1986.

760 Warren, S. G., Hahn, C. J., London, J., Chervin, R. M., and Jenne, R.: Global distribution of  
 761 total cloud cover and cloud type amount over land, Tech. Rep. Tech. Note TN-317 STR,  
 762 NCAR, 1988.

763 Weber, T., and Quaas, J.: Incorporating the subgrid-scale variability of clouds in the  
 764 autoconversion parameterization using a PDF-scheme, *J. Adv. Model. Earth Syst.*, 4,  
 765 M11003, doi:10.1029/2012MS000156, 2012.

766 Wielicki, B. A., Cess, R. D., King, M. D., Randall, D. A., and Harrison, E. F.: Mission to planet  
 767 Earth: Role of clouds and radiation in climate, *Bull. Amer. Meteor. Soc.*, 76, 2125–2153,  
 768 doi:10.1175/1520-0477(1995)076<2125:MTPERO.2.0.CO;2, 1995.

769 Wood, R., Field, P. R., and Cotton, W. R.: Autoconversion rate bias in stratiform boundary  
 770 layer cloud parameterization. *Atmos. Res.*, 65, 109–128, 2002.

771 Wood, R.: Drizzle in stratiform boundary layer clouds. Part I: Vertical and horizontal structure,  
 772 *J. Atmos. Sci.*, 62, 3011–3033, 2005a.

773 Wood, R.: Drizzle in stratiform boundary layer clouds. Part II: Microphysical aspects, *J.*  
 774 *Atmos. Sci.*, 62, 3034–3050, 2005b.

775 Wood, R. and Hartmann, D.: Spatial variability of liquid water path in marine low cloud: The  
 776 importance of mesoscale cellular convection, *J. Climate*, 19, 1748–1764, 2006.

777 Wood, R.: Cancellation of aerosol indirect effects in marine stratocumulus through cloud  
 778 thinning. *J. Atmos. Sci.*, 64, 2657–2669, 2007.

779 Wood, R.: Stratocumulus Clouds, *Mon. Wea. Rev.*, 140, 2373–2423. doi:  
 780 <http://dx.doi.org/10.1175/MWR-D-11-00121.1>, 2012.

781 Wood, R., Wyant, M., Bretherton, C. S., Rémillard, J., Kollias, P., Fletcher, J., Stemmler, J.,  
 782 deSzoeko, S., Yuter, S., Miller, M., Mechem, D., Tselioudis, G., Chiu, C., Mann, J.,  
 783 O'Connor, E., Hogan, R., Dong, X., Miller, M., Ghate, V., Jefferson, A., Min, Q., Minnis,  
 784 P., Palinkonda, R., Albrecht, B., Luke, E., Hannay, C., Lin, Y.: Clouds, Aerosol, and

Precipitation in the Marine Boundary Layer: An ARM Mobile Facility Deployment, Bull. Amer. Meteorol. Soc., doi: <http://dx.doi.org/10.1175/BAMS-D-13-00180.1>, 2015.

Wu, P., Dong, X. and Xi, B.: Marine boundary layer drizzle properties and their impact on cloud property retrieval, Atmos. Meas. Tech., 8, 3555–3562. doi: 10.5194/amt-8-3555-2015, 2015.

Wu, P., Dong, X., Xi, B., Liu, Y., Thieman, M., and Minnis, P.: Effects of environment forcing on marine boundary layer cloud-drizzle processes, J. Geophys. Res. Atmos., 122, 4463–4478, doi:10.1002/2016JD026326, 2017.

Xie, X., and Zhang, M.: Scale-aware parameterization of liquid cloud inhomogeneity and its impact on simulated climate in CESM, J. Geophys. Res. Atmos., 120, 8359–8371, doi:10.1002/2015JD023565, 2015.

Yoo, H., and Li, Z.: Evaluation of cloud properties in the NOAA/NCEP Global Forecast System using multiple satellite products. Climate Dyn., 39, 2769–2787, doi:10.1007/s00382-012-1430-0, 2012.

Yoo, H., and Li, Z., Hou, Y.-T., Lord, S., Weng, F., and Barker, H. W.: Diagnosis and testing of low-level cloud parameterizations for the NCEP/GFS using satellite and ground-based measurements. Climate Dyn., 41, 1595–1613, doi:10.1007/s00382-013-1884-8, 2013.

Zhang, J., Lohmann, U., and Lin, B.: A new statistically based autoconversion rate parameterization for use in large-scale models. J. Geophys. Res., 107, 4750, doi:10.1029/2001JD001484, 2002.

Zhang, Z., Song, H., Ma, P.-L., Larson, V., Wang, M., Dong, X., and Wang, J.: Subgrid variations of cloud water and droplet number concentration over tropical oceans: satellite observations and implications for warm rain simulation in climate models. Submitted to Atmos. Chem. Phys., 2018.



810 **Table 1. The parameters of autoconversion and accretion formulations for four**  
811 **parameterizations.**

	$A$	$a1$	$a2$	$B$	$b$
Khairoutdinov and Kogan (2000)	1350	2.47	-1.79	67	1.15
	$1.3 \times 10 \beta_6^6$ , where $\beta_6^6 = [(r_v + 3)/r_v]^2$ , $r_v$ is mean volume radius.				
Liu and Daum (2004)		3	-1	N/A	N/A
	modification was made by Wood (2005b)				
Tripoli and Cotton (1980)	3268	7/3	-1/3	1	1
Beheng (1994)	$3 \times 10^{34}$ for $N_c < 200 \text{ cm}^{-3}$ $9.9$ for $N_c > 200 \text{ cm}^{-3}$	4.7	-3.3	1	1

813

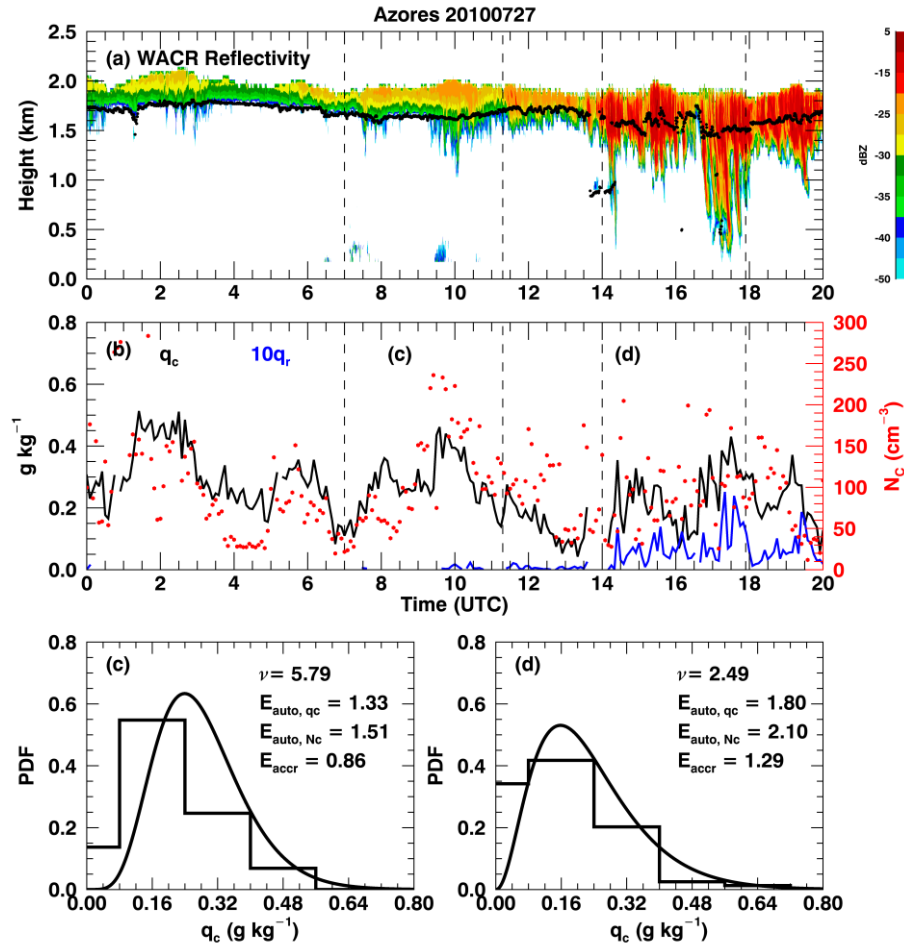
814 **Table 2. Autoconversion (left) and accretion (right) enhancement factors in different**  
815 **boundary layer conditions (LTS > 18 K for stable, LTS < 13.5 K for unstable and LTS**  
816 **within 13.5 and 18 K for mid-stable) and in different LWP regimes (LWP  $\leq 75$  g m<sup>-2</sup> for**  
817 **non-precipitating and LWP > 75 g m<sup>-2</sup> for precipitating).**

LTS (K)	LWP $\leq 75$ g m <sup>-2</sup>	LWP > 75 g m <sup>-2</sup>
> 18	2.32/1.42	2.75/1.52
(13.5, 18)	2.61/1.47	3.07/1.68
< 13.5	4.62/1.72	6.94/1.86

819

**Table 3. Autoconversion and accretion enhancement factors ( $E_{auto}$  and  $E_{accr}$ ) for the parameterizations in Table 1 except the Khairoutdinov and Kogan (2000) scheme. The values are averaged for 60-km and 180-km model grids.**

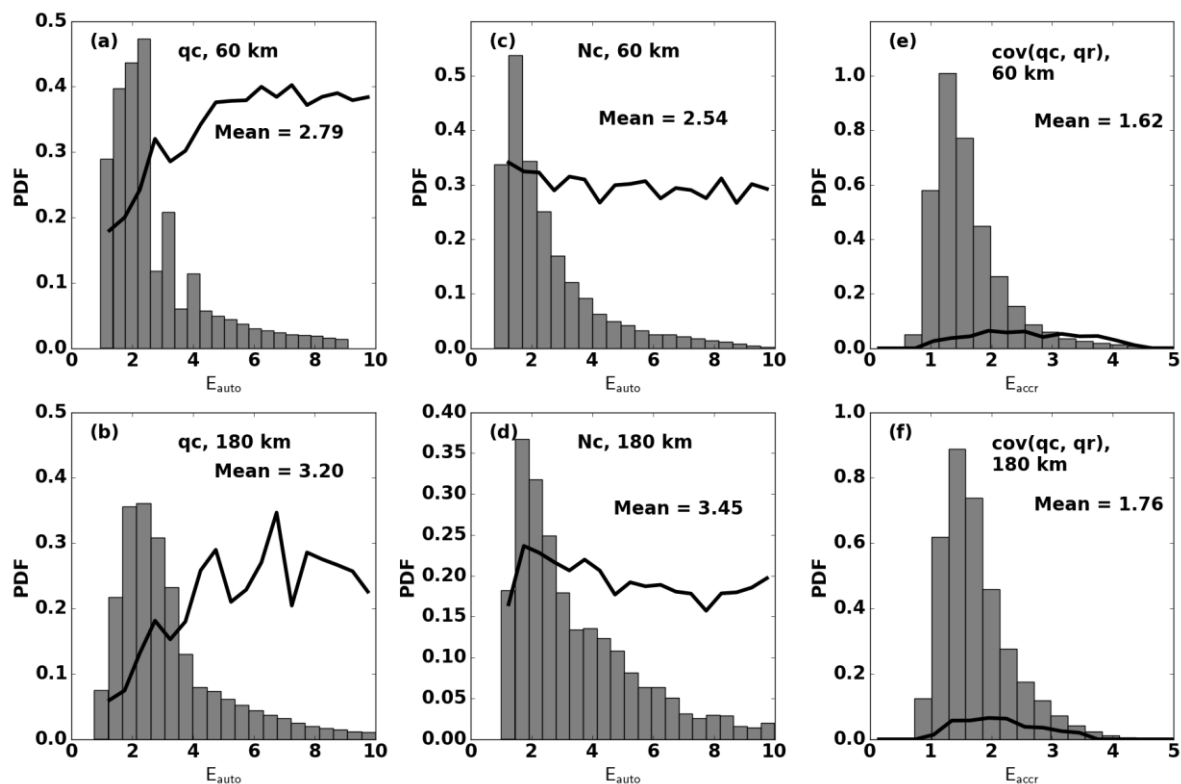
	$E_{auto}$		$E_{accr}$	
	60-km	180-km	60-km	180-km
Liu and Daum (2004)	3.82	4.23	N/A	N/A
Tripoli and Cotton (1980)	2.46	2.69	1.47	1.56
Beheng (1994)	6.94	5.88	1.47	1.56



825

826 **Figure 1. Observations and retrievals over Azores on 27 July 2010. (a) W-band ARM**  
 827 **cloud radar (WACR) reflectivity (contour) superimposed with cloud-base height (black**  
 828 **dots). (b) Black line represents averaged cloud water mixing ratio ( $q_c$ ) within the top five**  
 829 **range gates, blue line represents averaged rain ( $\times 10$ ) water mixing ratio within five range**  
 830 **gates around maximum reflectivity, red dots are the retrieved cloud droplet number**  
 831 **concentration ( $N_c$ ). Dashed lines represent two periods that have 60 km model grids with**  
 832 **similar mean- $q_c$  but different distributions as shown by step lines in (c) and (d). Curved**  
 833 **lines in (c) and (d) are fitted gamma distributions with the corresponding shape**  
 834 **parameter ( $\nu$ ) shown on the upper right.  $N_c$  distributions are not shown. The calculated**  
 835 **autoconversion ( $E_{\text{auto}, q_c}$  from  $q_c$  and  $E_{\text{auto}, N_c}$  from  $N_c$ ) and accretion ( $E_{\text{accr}}$ ) enhancement**  
 836 **factors are also shown.**

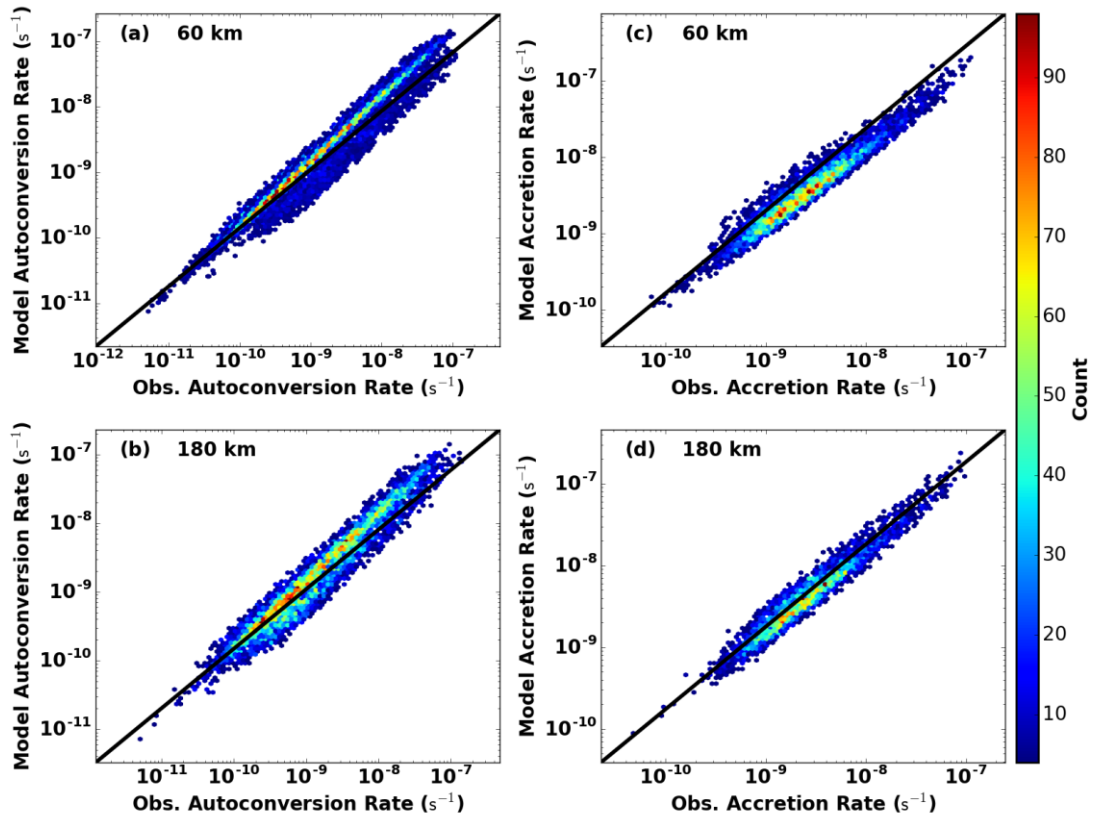
837  
838



839

840 **Figure 2. Probability density functions (PDFs) of autoconversion (a - d) and accretion (e**  
 841 **- f) enhancement factors calculated from  $q_c$  (a-b),  $N_c$  (c-d), and the covariance of  $q_c$  and**  
 842  **$q_r$  (e-f). The two rows show the results from 60-km and 180-km model grids, respectively,**  
 843 **with their average values. Black lines represent precipitation frequency in each bin in (a)-**  
 844 **(d) and the ratio of layer-mean  $q_r$  to  $q_c$  in (e)-(f).**

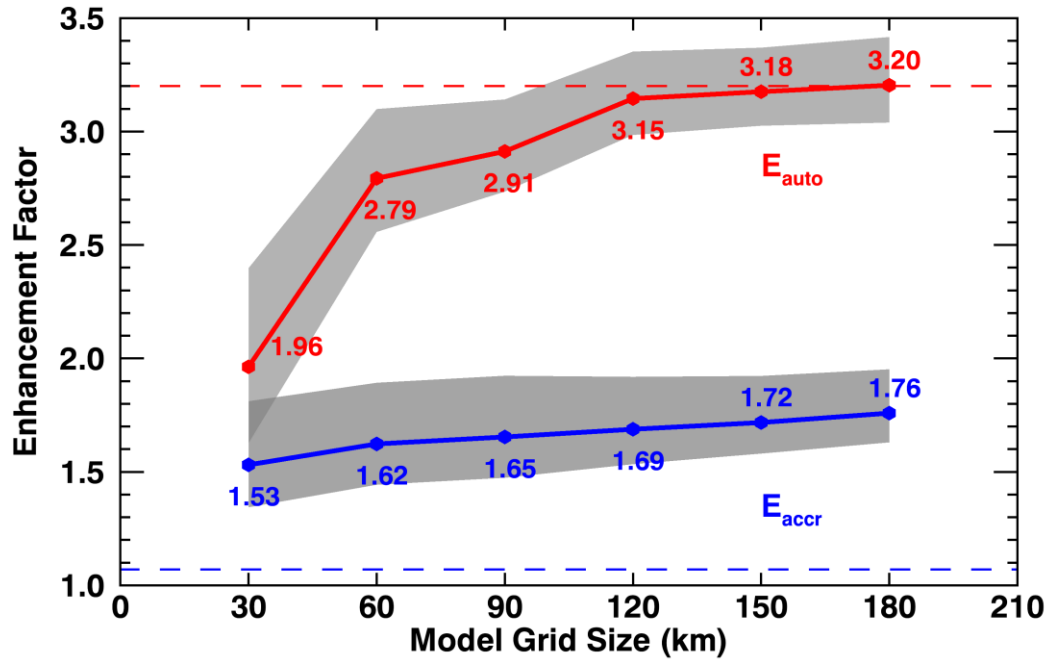
845



846

847 **Figure 3.** Comparison of autoconversion (a-b) and accretion (c-d) rates derived from  
848 observations (x-axis) and from model (y-axis). Results are for 60-km (a and c) and 180-  
849 km model grids. Colored dots represent joint number densities.

850



851 **Figure 4.** Autoconversion (red line) and accretion (blue line) enhancement factors as a  
852 function of model grid sizes. The shaded areas are calculated by varying  $q_c$  and  $q_r$  within  
853 their retrieval uncertainties. The two dashed lines show the constant values of  
854 autoconversion (3.2) and accretion (1.07) enhancement factors prescribed in MG08.

855

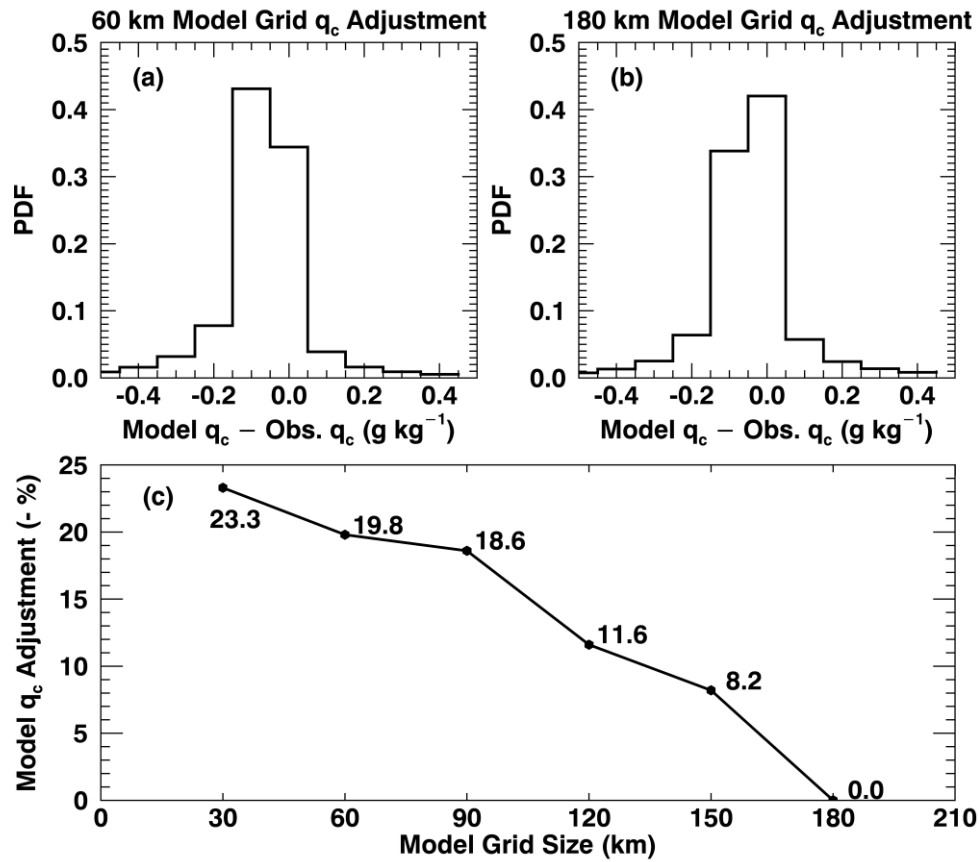
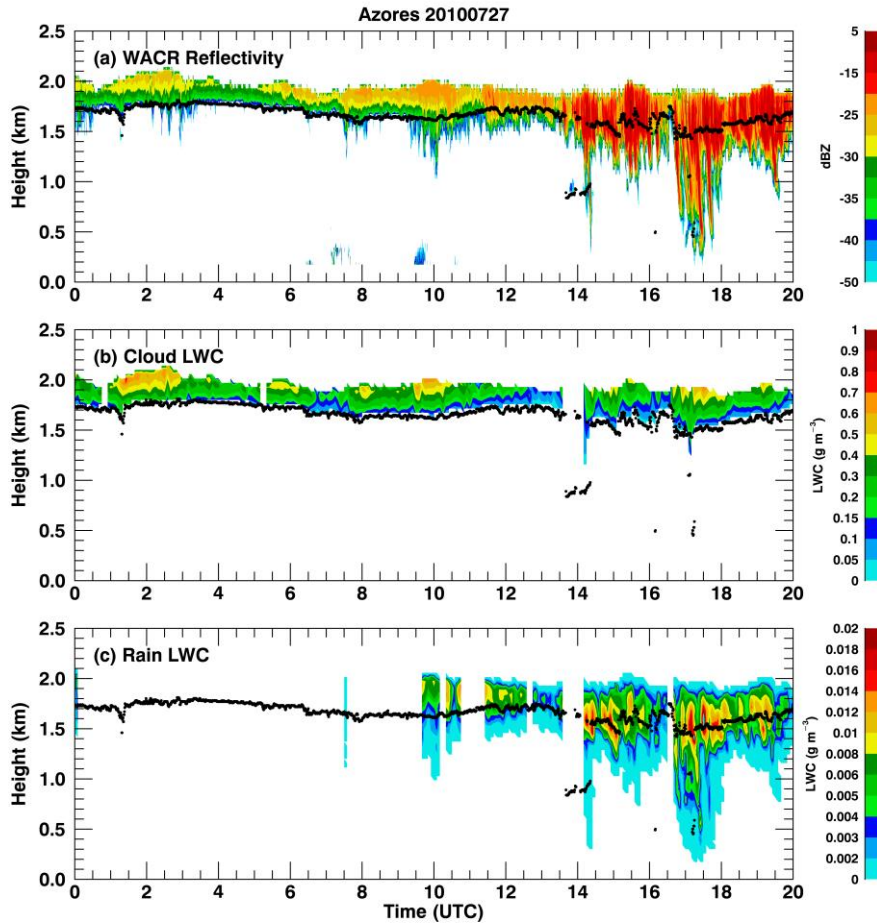


**Figure 5.  $q_c$  needed for models to adjust to reach the same autoconversion rate as observations for (a) 60-km and (b) 180-km model grids. Positive biases represent increased  $q_c$  are required in models and negative biases mean decreased  $q_c$ . The average percentages of adjustments for different model grid sizes are shown in panel (c) and note that the percentages in the vertical axis are negative.**





863

864 **Figure A1. Joint retrieval of cloud and rain liquid water content (CLWC and RLWC) for**  
865 **the same case as in Figure 1. (a) WACR reflectivity, (b) CLWC, and (c) RLWC. The black**  
866 **dots represent cloud base height. Blank gaps are due to the data from one or more**  
867 **observations are not available or reliable. For example, the gap before 14 UTC is due to**  
868 **multiple cloud layers are detected whereas we only focus on single layer cloud.**